ACS APPLIED NANO MATERIALS

www.acsanm.org Article

Nanoscale Surface Structure of Nanometer-Thick Ferroelectric $BaTiO_3$ Films Revealed by Synchrotron X-ray Scanning Tunneling Microscopy: Implications for Catalytic Adsorption Reactions

Pedram Abbasi, Nozomi Shirato, Rishi E. Kumar, Isabel V. Albelo, Matthew R. Barone, Deniz N. Cakan, Ma. de la Paz Cruz-Jáuregui, Sarah Wieghold, Darrell G. Schlom, Volker Rose, Tod A. Pascal,* and David P. Fenning*

Cite This: https://doi.org/10.1021/acsanm.2c05257 Read Online

ACCESS | Metrics & More | Article Recommendations | Supporting Information

ABSTRACT: Ferroelectric nanomaterials are of interest in catalysis, nonvolatile memory, and neuromorphic computing among other applications because of their switchable structure that can alter the electronic and interface properties of a single material. The investigation of the role of polarization on the surface structure and chemistry of ferroelectric nanomaterials is a longstanding challenge, as it ideally requires a combination of both nanoscale imaging and chemical spectroscopy. In this work, we study a model ferroelectric $BaTiO_3$ thin film by synchrotron X-ray scanning tunneling microscopy (SX-STM), a unique method that integrates nanoscale surface imaging and chemically sensitive spectroscopy. We find that polarization switching from downward to upward in (001) single-crystalline $BaTiO_3$ thin films increases the intensity of X-ray absorption across Ba *M*, Ti *L*, and O *K* edges. Chemical mapping of nanometer-sized domains further demonstrates the modulation of surface structures upon polarization switching, as well as confirming the trends observed in single-point experiments across the surface. We complement these measurements with *ab initio* computational absorption spectroscopy to elucidate the effect of polarization switching on the core−hole excitations using the Bethe−Salpeter equation approach. Our experimental and theoretical results thus confirm a stronger binding strength for the upward-polarized surface with molecular O_2 as a model reactant, offering mechanistic evidence that supports previous reports. This work advances the understanding of the surface chemistry and electronic structure of ferroelectrics, which can ultimately aid strategies to design interfaces with tailored properties.

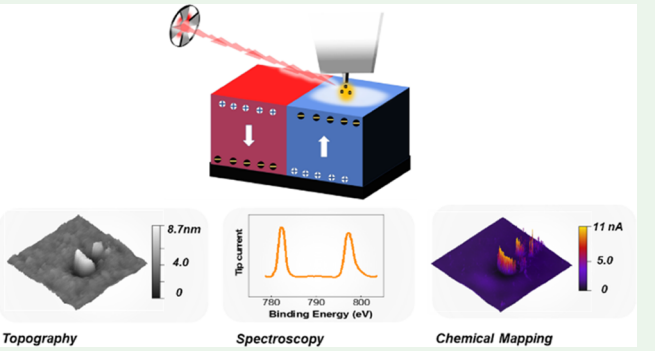

KEYWORDS: *ferroelectrics, X-ray absorption spectroscopy, scanning tunneling microscopy, density functional theory, catalysis*

INTRODUCTION

For more than a century, ferroelectrics have been of interest for a wide range of applications including data storage, sensors, and energy harvesting, as the presence of two or more stable polar phases offers an array of possible enhancements in these technologies.[1] Since 1980, advances in nanotechnology and thin film synthesis have led to extensive implementation of ferroelectric single crystals in electronics including semiconductor chips,[2] nonvolatile memories,[3] field-effect transistors,[4] and a variety of micro-electromechanical systems.[5] It was soon realized that tuning ferroelectric layers in heterojunctions and superlattices can add significant functionality to even more diverse architectures, which has in turn triggered extensive research on the interfacial properties of ferroelectrics.[6] A focus on interfaces led to an intense investigation of ferroelectrics in related fields, including photovoltaics[7,8] and catalysis,[9−13] where switchable interface properties are of significant importance. Throughout, a critical challenge in investigating ferroelectric interfaces has remained the simultaneous probing of the effect of polarization on both surface structure and chemistry at the atomic scale. To date, scanning probe microscopy (SPM) techniques, such as scanning tunneling microscopy (STM)[14,15] and piezoresponse force microscopy (PFM),[16,17] have been used to investigate the effect of ferroelectricity on surface topography and ferroelectric state down to the sub-nanometer level. These techniques, however, provide limited insight into the chemical fingerprints of the surface structure upon polarization switching. As a result, these techniques are usually coupled to secondary imaging or

Received: December 9, 2022
Accepted: January 4, 2023

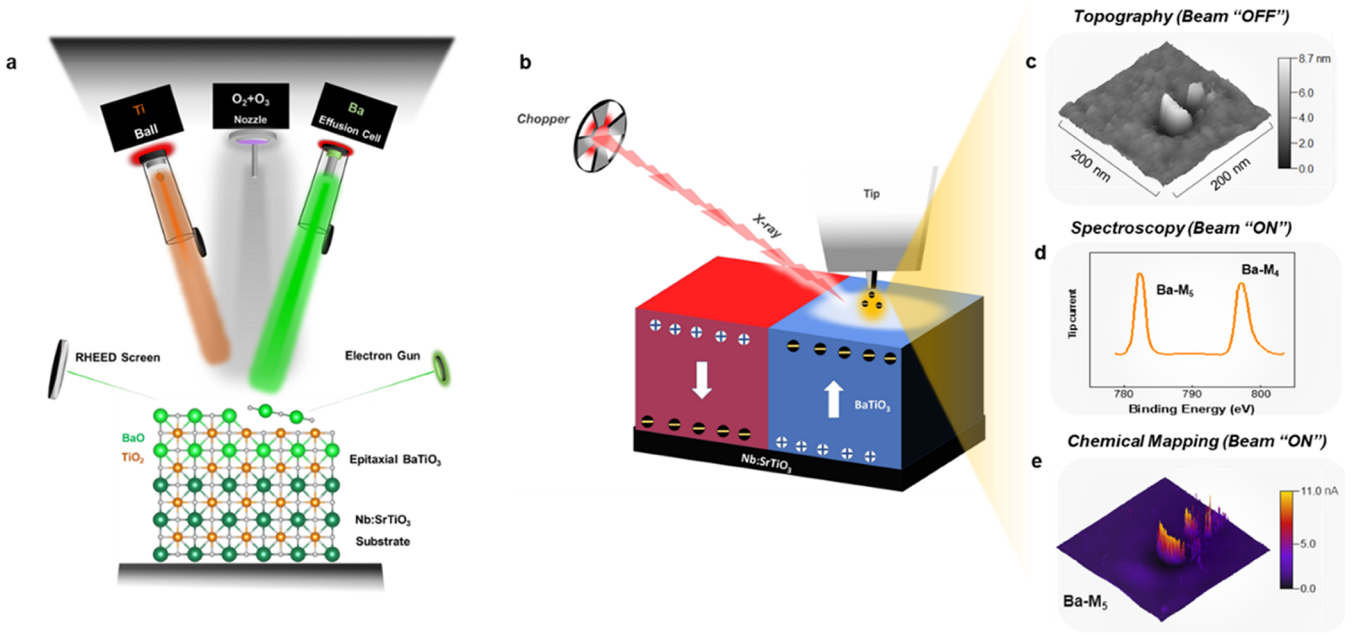

Figure 1. Introduction to the MBE synthesis method and SX-STM technique. (a) Schematic of MBE chamber with a Ti ball source, Ba Knudsen effusion cells, and O_2/O_3 source during the growth of a BaO monolayer on the surface of epitaxial $BaTiO_3$ on the Nb:$SrTiO_3$ substrate. Ba, Ti, Sr, and O atoms are shown in light green, orange, dark green, and gray, respectively. (b) Schematic of a polarized $BaTiO_3$ film tunneling photoelectrons to the STM tip in near-field mode. (c) Schematic of a three-dimensional (3D) topographical map obtained in the beam "OFF" mode. (d) Schematic of XAS spectra obtained from the point of interest in spectroscopy mode. (e) Schematic of an elemental map obtained in the beam "ON" mode from the same area resolving surface chemistry.

spectroscopic methods, such as photoemission electron microscopy (PEEM),[18] electron energy loss spectroscopy (EELS),[19] X-ray photoelectron spectroscopy (XPS),[16] or X-ray absorption spectroscopy (XAS),[20] to provide information on the chemistry and electronic structure of the surface. However, most of these secondary techniques only provide an average response over a surface volume of a few microns in length and at least several unit cells in depth, limiting true surface sensitivity with atomic resolution. Another drawback in implementing independent techniques to investigate ferroelectric effects on the surfaces, especially as it relates to catalysis, is establishing the identical polarization state on the surface for a reliable comparison of the results across different experiments, highlighting the importance of *in situ* polarization switching.[21] Among recent efforts in addressing this issue, only cross-sectional transmission electron microscopy (TEM)[22−24] and scanning TEM (STEM)[25−28] with *in situ* biasing have been shown to be capable of providing an in-depth understanding of the surface structure and chemical shifts with atomic resolution.

In this report, we use a combination of synchrotron X-ray scanning tunneling microscopy (SX-STM)[29,30] and *ab initio* XAS calculations to investigate the effect of out-of-plane polarization switching on the morphology, chemical composition, and surface reactivity of model epitaxial ferroelectric $BaTiO_3$ thin films. SX-STM combines the chemical fingerprinting of the surface by X-ray spectroscopy with the high spatial resolution of STM and the possibility of gas dosing to the surface. The use of chopped X-ray illumination permits discrimination of topographical and chemical fingerprints at the surface with atomic resolution.[31] Moreover, an STM "smart tip"[30] enables *in situ* biasing of the surface for polarization switching. In conjunction with the synchrotron-based XAS experiments, we performed *ab initio* core-excited XAS calculations based on the Bethe−Salpeter equation (BSE)[32,33] using the *OCEAN*[34] code to quantify the effect of polarization switching on the electronic structure of both ground and excited states of the studied atomic sites. Implementation of the BSE method, which includes many-body perturbation[35] effects, enables us to capture the interplay between polarization and lattice distortion at the atomic scale, including complex physics (such as spin−orbit coupling[36]) at the surface seen in the experimental measurements. Combining the unique capabilities of SX-STM with computational absorption spectroscopy and insights from *ab initio* calculations thus enables a deeper understanding of the role of polarization switching on nanoscale interface properties.

RESULTS AND DISCUSSION

Epitaxial single-crystal (001)-oriented $BaTiO_3$ thin films (∼15 nm thick) were synthesized by molecular-beam epitaxy (MBE)[37] on Nb-doped $SrTiO_3$ (NSTO) substrates (Figure 1a). $SrTiO_3$ is a well-established substrate for growing epitaxial $BaTiO_3$ due to its suitable lattice mismatch (∼2%) enhancing tetragonality (and therefore out-of-plane polarization) in the MBE-grown films.[38] Moreover, in our films, Nb-doped $SrTiO_3$ acts as a conductive back-contact necessary for achieving polarization switching when biasing the surface with the STM tip. During growth, elemental barium and titanium were supplied by a conventional effusion cell and a Ti ball,[39] respectively, while the background pressure was 5×10^{-7} Torr of (O_2 + 10% O_3) and the substrate temperature was kept at 850 °C.

Reciprocal space maps (RMS) and X-ray diffraction (XRD) (Figure S1) confirm that the films are of high quality, *c*-axis oriented, and commensurately strained. Piezoresponse force microscopy (PFM) was then used to verify the ferroelectric response as well as the coercive field in the as-grown samples.

https://doi.org/10.1021/acsanm.2c05257
ACS Appl. Nano Mater. XXXX, XXX, XXX−XXX

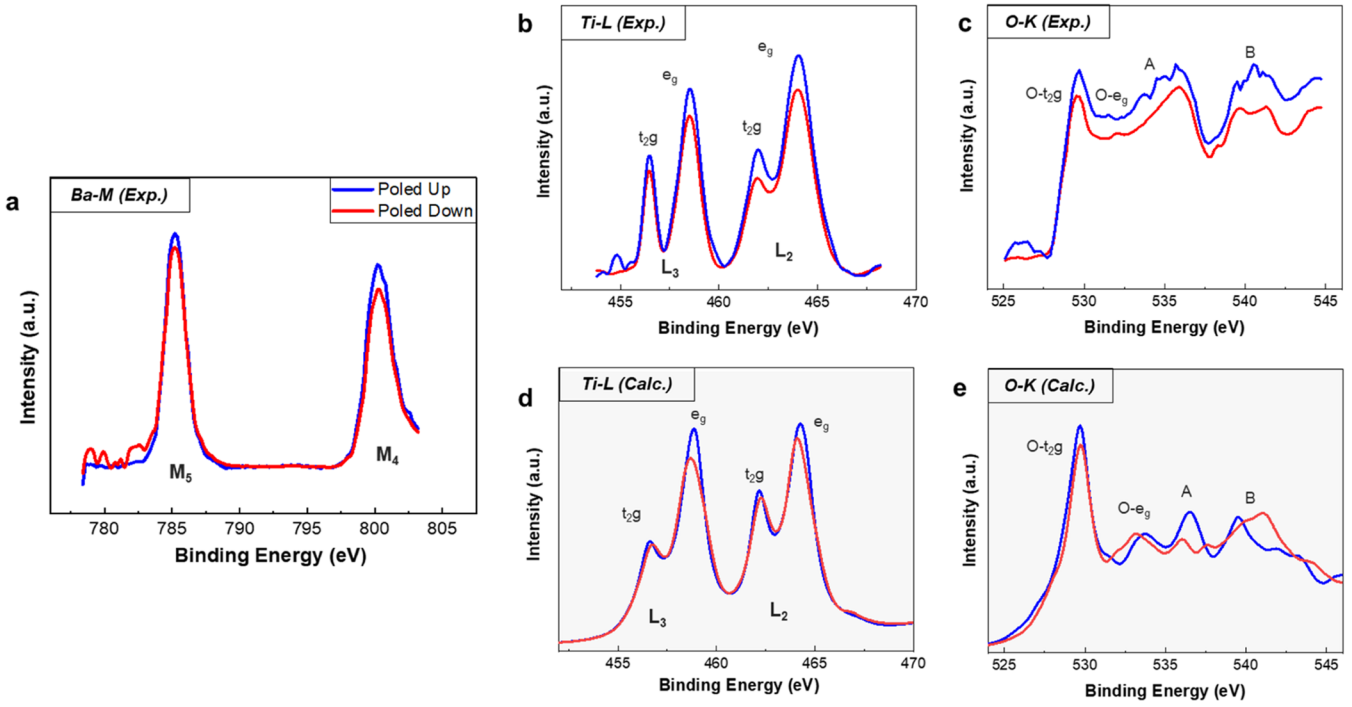

Figure 2. Effect of ferroelectric polarization switching on the absorption spectra based on SX-STM and computational BSE approach. (a) Ba *M*, (b) Ti *L*, and (c) O *K* edge results from SX-STM compared with (d) Ti *L* and (e) O *K* edges results obtained from *ab initio* XAS calculation.

The results (Figure S2) show that films have an ultrasmooth surface with an RSM value of 1.8 Å. The writing of upward and downward domains by the PFM tip confirms the ferroelectric nature of the films as well as a coercive voltage of less than ±3 V (Figure S2). This modest coercive voltage is critical to enable *in situ* biasing with the STM tip during SX-STM measurements to achieve local polarization reversal on the surface of the films.

Figure 1b shows a schematic of the SX-STM setup used for this study. A specific area of the sample is first polarized by applying a bias between the sample and STM tip, then irradiated with X-rays to generate photoelectrons. These photoelectrons are collected via tunneling to the tip in the near-field mode, where the tip−sample distance is ∼1 nm.

The total tunneling current in SX-STM measurements is the sum of both the standard STM tunneling current and an X-ray excited photoelectron current collected at the tip:

$$I_{\text{SX-STM}} = I_{\text{tunneling(dark)}} + I_{\text{tunneling(X-ray)}} \quad (1)$$

Here, $I_{\text{tunneling (dark)}}$ is the conventional tunneling current controlled by a feedback loop and $I_{\text{tunneling (X-ray)}}$ is the X-ray excited/enhanced tunneling current generated from tunneling electrons being boosted by X-ray irradiation under the tip. $I_{\text{tunneling (dark)}}$ provides the morphology information about the sample surface similar to traditional STM, while $I_{\text{tunneling (X-ray)}}$ provides the local chemical information. Simultaneous capturing of these two modalities is enabled by implementing an ultrahigh-vacuum optical chopper in the experimental setup creating both dark-mode (beam "OFF") topographical mapping (corresponding to $I_{\text{tunneling (dark)}}$) (Figure 1c) and beam "ON" mode (corresponding to both $I_{\text{tunneling (dark)}}$ + $I_{\text{tunneling (X-ray)}}$) chemical maps for the areas of interest (Figure 1d). SX-STM thus enables two additional modalities of spectral data collection, each sensitive mainly to surface atoms as discussed below:

Element-Specific, Single-Point XAS. In this mode, measurements are executed by taking the X-ray-induced tip/sample current (in TEY mode) as a function of varying X-ray energy, when the tip stays in the tunneling regime (Figure 1d).[29] It is important to note that the much smaller interaction volume for STM in tunneling enables state-of-the-art lateral resolution for single-point XAS measurements (<10 nm depending on surface quality and tip condition), which is several orders of magnitude higher than traditional techniques (which typically have resolutions of 10−100 μm[40]) and is extremely surface sensitive.

Surface Chemical Mapping. Chemical mapping is performed by collecting the tip/sample current as a function of lateral displacement at constant X-ray energy, similar to conventional STM tip raster-scanning experiments. The current reflects the local chemical nature of the material as the tip rasters across the surface (Figure 1e). Topographical maps can therefore be retrieved based on $I_{\text{tunneling (dark)}}$, while chemical maps independent from topographical variations can be achieved by subtracting $I_{\text{tunneling(dark)}}$ from the total tunneling current ($I_{\text{SX-STM}}$) based on eq 1. It should be noted that, compared with single-point XAS, in this mode, the resolution of the maps is determined by a combination of imaging/instrumental artifacts, i.e., tip condition, background noise, drift, etc., and the intrinsic limit due to surface conditions and quantum mechanical interactions, i.e., surface quality, roughness, and element-specific excitations.[30,31]

More details on the experimental setup are provided in the Supporting Information (SI).

The effect of ferroelectric polarization on the absorption spectra of $BaTiO_3$ films was investigated by pre-biasing a single area of the $BaTiO_3$ surface followed by single-point, XAS measurements at the Ba *M*, Ti *L*, and O *K* edges. These experimental spectra were complemented by *ab initio* XAS calculations as shown in Figure 2.

https://doi.org/10.1021/acsanm.2c05257
ACS Appl. Nano Mater. XXXX, XXX, XXX−XXX

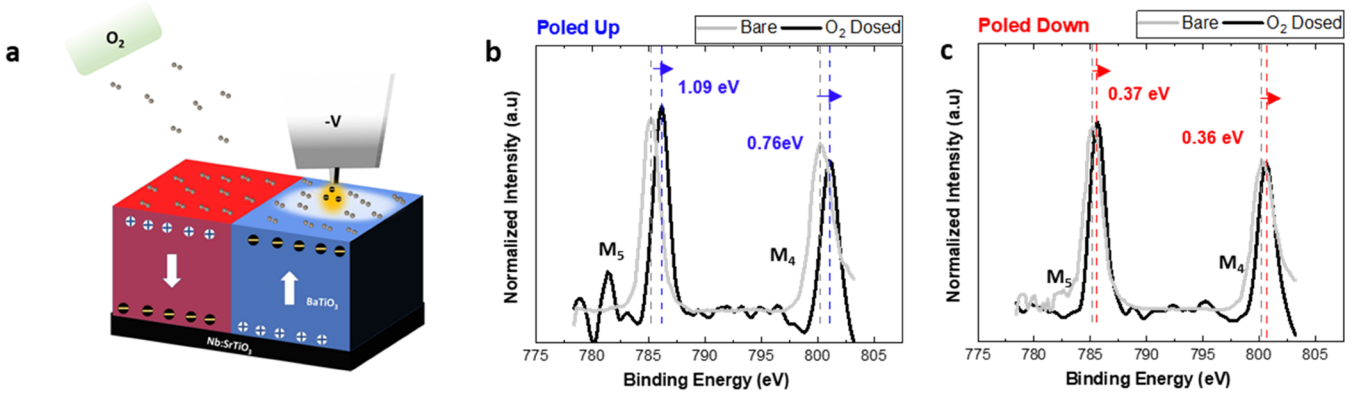

Figure 3. Effect of O_2 adsorption on the Ba *M* XAS spectra. (a) Schematic of O_2 dosing experiment on pre-poled areas on the sample. (b) Comparison of Ba *M* XAS spectra on bare and O_2 dosed surfaces with upward polarization and (c) downward polarization.

Both the SX-STM and computational XAS show evidence of a decrease in absorption upon switching from the upward to downward polarization states, across all three edges studied (Figure 2). The consistent decrease at different edges suggests a clear effect of ferroelectric polarization on the number of photoelectrons emitting from the surface to the tip in tunneling mode. Previously, a downward polarization in ferroelectric $BaTiO_3$ thin films was shown to lead to a decreased electron density at the surface of the films due to an upward band bending.[12] Therefore, a decreased probability for tunneling of photoelectrons at the downward-poled surface may underlie the consistent decrease in X-ray absorption across all three edges.

Apart from the overall change in the relative XAS intensities, SX-STM and computational results obtained by the BSE method on Ti L and O K (Figure 2b–e) edges show that ferroelectric switching has the most pronounced effect on the e_g peaks.[41,42] The Ti *L*-edge spectra show the expected separation between the L_3 and L_2 edges, attributed to excitations from Ti $2p_{3/2}$ (L_3) and $2p_{1/2}$ (L_2) states. Crystal field splitting of the 3d band further splits these two states into sub-bands of t_{2g} with peaks at 456.4 and 461.93 eV and e_g with peaks at 458.53 and 464.06 eV, showing a good agreement with previous experimental results.[20] Here, the t_{2g} states are associated with d_{xy}, d_{xz}, or d_{yz} orbital pointing sideways with O 2p orbitals, while e_g states are associated with d_z^2 and $d_{x-y}^{2\ 2}$ orbitals pointing directly toward the O 2p states. This direct interaction explains the higher sensitivity of e_g states to the displacement of the Ti ion within the TiO_6 octahedron.[43,44]

Experimental results on the Ba $M_{5,4}$ edge (Figure 2a) show a greater branching (M_5/M_4) ratio for the poled-down state. Narrow XAS scans at the Ba $M_{5,4}$ edge show two sharp peaks at 785.27 and 800.15 eV associated with excited electrons originating at Ba $3d_{5/2}$ and $3d_{3/2}$, respectively. It has previously been reported that a stronger spin–orbit coupling leads to a higher branching ratio in transition metal oxides.[45] The higher M_5/M_4 branching ratio may suggest a stronger spin–orbit coupling for the downward-poled surface.

XAS of the O *K* edge is presented in Figure 2c,e, showing two primary features at 529.45 and 531.5 eV attributed to hybridization between O 2p states with Ti 3d-t_{2g} and Ti 3d-e_g orbitals, respectively. Two other peaks labeled as A and B are attributed to higher-order scattering effects as well as the influence of Ba d and f orbitals on the empty O 2p density of states and are of less relevance to our model, since here we are mainly considering the effect of lattice distortion in Ti d and O 2p orbitals associated with *c*-axis polarization.[43,46]

Overall, our computational XAS of the Ti *L* and O *K* edges shows good agreement with our experimental observations of $L_{2,3}$ splitting, the ratio of t_{2g} to e_g sub-bands, and stronger modulation on e_g states. Our calculations thus quantify the effect of ferroelectric switching on the electronic states, as manifest in the relative peak intensities, orbital hybridization, and crystal field and spin–orbit coupling. It is worth noting that computational modeling of the core-excitation dependence on ferroelectric polarization in transition metal oxides and perovskites is a challenging task due to the spin–orbit coupling and other strong multiplet effects;[34,47,48] to the best of our knowledge, our work is the first study that computationally incorporates such physics to elucidate the electronic structure of this class of material system.

Given that XAS is sensitive to the surface electronic structure and chemistry upon polarization switching, we further investigated the interaction of these two polarized surfaces with a model adsorbate. Based on our previous laboratory XPS study of the valence and core-level spectra of $BaTiO_3$, we expect the Ba *M* edge to have a high sensitivity to both polarization switching and surface oxidation state.[12] Therefore, here we focused on the Ba *M* edge to investigate the effect of polarization switching on O_2 adsorption. Two different areas of the samples were first polarized in upward and downward states and then dosed with O_2 molecules at 2.5×10^{-6} Torr for 10 min.

The Ba *M* edge XAS spectra after O_2 dosing show a clear shift of both Ba M_5 and M_4 peaks to higher binding energies with the upward-polarized surface, showing a greater shift on both edges (Figure 3). The overall shift to higher binding energies upon O_2 adsorption confirms oxidation (i.e., some loss in electron density) of the surface Ba sites in both polarization states. Furthermore, the poled-up surface shows a larger shift than the poled-down surface (a shift of 1.09 vs 0.37 eV for the M_5 edge and 0.76 vs 0.36 eV for the M_4 edge for the poled-up surface vs. poled-down surface, respectively). This shows that the poled-up surface has a stronger interaction with O_2 molecules and a greater degree of oxidation relative to the poled-down surface. The greater oxidation of the poled-up surface is in line with our findings in Figure 2, exhibiting a larger electron density at the surface available for chemisorption interaction with O_2.

To further investigate the interaction of O_2 molecules with $BaTiO_3$ surfaces, we performed *ab initio* DFT calculations,

https://doi.org/10.1021/acsanm.2c05257
ACS Appl. Nano Mater. XXXX, XXX, XXX–XXX

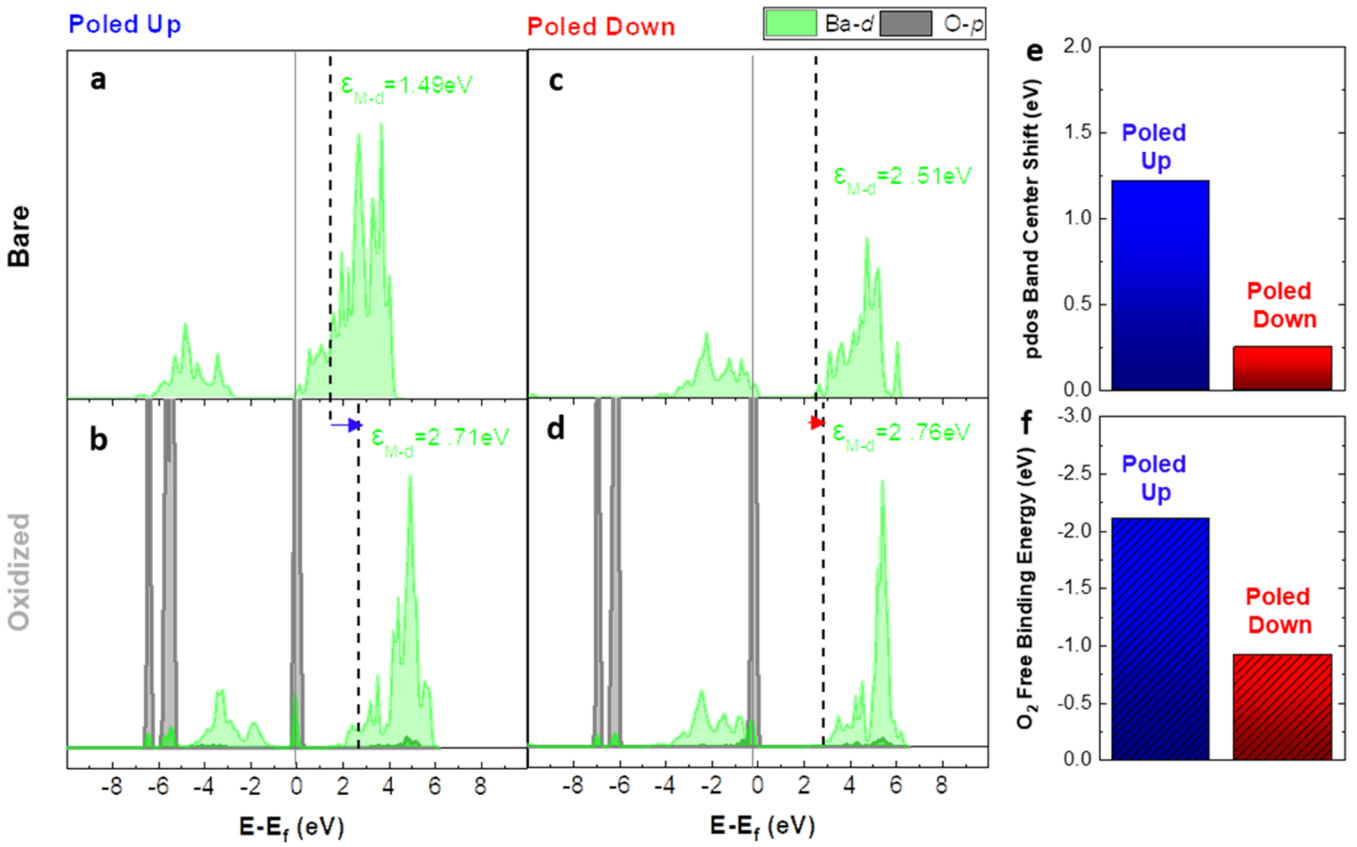

Figure 4. Effect of O_2 adsorption on polarized $BaTiO_3$ slabs based on *ab initio* DFT + *U* calculations. (a, b) Density of states for Ba d and O p states on bare and oxidized slabs with upward polarization and (c, d) downward polarization. (e) Extent of Ba d-band center shifts due to oxidation. (f) O_2 free binding energy on Ba site of poled-up and poled-down slabs.

using the GGA + *U* approximation on polarized slab models. The computational results shown in Figure 4 confirm a stronger hybridization and greater electron exchange on the poled-up surface compared with the poled-down one. Partial density of states calculations of the bare surfaces (without any O_2 adsorbed) in Figure 4a,c shows that the Fermi level for the poled-up surface is closer to the conduction band and overlaps with the valence band than for the poled-down surface, i.e., the poled-up surfaces are electron-doped while the poled-down surfaces are hole-doped. Comparing these two slab models after O_2 adsorption, we find an upshift of d-band centers (ϵ_d) as the surface becomes more hole-doped due to hybridization with O p orbitals. Moreover, the extent of ϵ_d shifts shows greater modulation for the poled-up surface compared with the poled-down surface (Figure 4e). These two effects are consistent with the positive shifts observed in Ba *M* binding energies in Figure 3 upon surface oxidation.

We further investigated the free binding energy of O_2 molecules to Ba surface sites. Our calculations show that the Ba sites on the upward-polarized surfaces have an O_2 free binding energy of −2.08 eV, which is larger than −0.78 eV of the downward-poled surface (Figure 4f). Moreover, the poled-down surfaces exhibit a larger density of electron displacement upon hybridization with O_2 molecules, evidenced by the exchange electron density iso-surfaces (Figure S4).

We investigated the effect of ferroelectric polarization switching on the surface reconstruction of ferroelectric $BaTiO_3$ films by performing chemical mapping across the Ba *M*, Ti *L*, and O *K* edges under two different polarization states, taking advantage of the unique capability of SX-STM to perform high-resolution chemical mapping (Figure 5). We aimed to determine whether *in situ* poling can lead to a local surface reconstruction or domain creation. Thus, we pre-biased a selected area of the surface with opposite polarization (up and down) and performed chemical mapping at one main-edge energy of each of the three Ba *M*, Ti *L*, and O *K* edges, as well as pre-edge energy for each element. To construct chemical maps, the intensity of each pixel at the main peak was normalized to its pre-edge intensity, enabling us to eliminate possible drifts and artifacts during measurements. (Further details of processing steps are presented in the SI.)

As we switch the polarization from downward to upward, we expect a change in tunneling current originating from (i) a different electron density at the surface and (ii) a different local structure based on chemical or morphological surface reconstruction. Here, any change in the physical morphology of the surface upon polarization switching is expected to be observed predominantly in the beam "OFF" dark/standard STM. On the other hand, any chemical or electronic contrast due to polarization switching is probed by a change in X-ray excited photoelectrons when the surface is illuminated by X-ray in the beam "ON" mode. Therefore, for an accurate investigation of surface chemical shifts upon polarization switching, we need to consider both dark-mode topographical maps and the additional contribution of X-ray-excited electrons on the dark-mode maps.

The results in Figure 5a−f show dark-mode-normalized maps of the surfaces with upward and downward polarizations at the three edges, and the panels a′−f′ show the normalized X-ray chemical maps with dark current subtracted. To further

https://doi.org/10.1021/acsanm.2c05257
ACS Appl. Nano Mater. XXXX, XXX, XXX−XXX

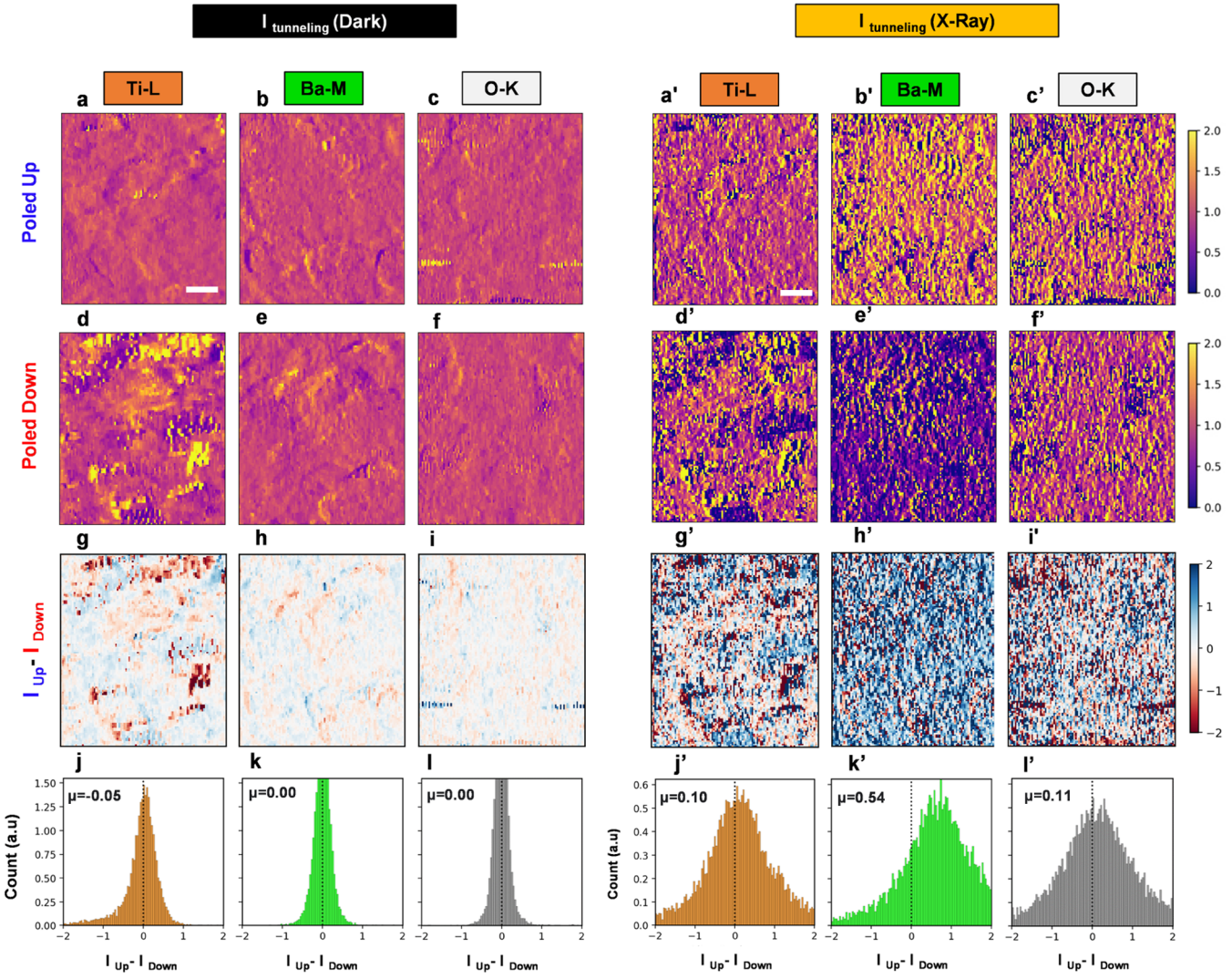

Figure 5. Effect of ferroelectric polarization switching on the surface chemical maps. Dark STM maps are taken from Ti *L*, Ba *M*, and O *K* edges of (a–c) upward- and (d–f) downward-polarized samples. (g–i) Contrast maps between the dark maps of upward and downward polarization slabs. (j–l) Statistical distribution of intensities from contrast maps. Chemical contribution of total current under X-ray illumination taken at Ti L, Ba M, and O K edges of (a′–c′) upward- and (d′–f′) downward-polarized samples. (g′–i′) Contrast maps based on the net chemical maps of upward- and downward-polarized samples. (j′–l′) Statistical distribution of intensities from contrast maps. Scale bar is 15 nm.

isolate the chemical contrast arising specifically from polarization switching, we took the difference of the signals from the poled-down and poled-up chemical maps. The maps and distributions of these differences are shown for each edge in Figure 5g–l,g′–l′. It is evident that polarization switching in dark STM maps leads to an undistinguishable contrast (Figure 5g–i) between poled-up and poled-down surfaces, with average contrast intensities close to zero (Figure 5j–l).

Irradiating the surface with X-ray clearly modulates dark STM maps across different edges (Figure 5a′–f′), demonstrating the role of photoelectron excitation in creating chemical contrast upon polarization switching. This substantial chemical contrast highlights the power of the SX-STM approach to resolving microscopic chemical changes at the surface separate from the morphology. The results shown in Figure 5g′–l′ show a positive chemical shift to higher intensities across the three studied edges, underscoring a coherent modulation on the surface chemistry upon polarization switching from downward to upward. These high-resolution maps are thus in line with our earlier observation in single-point spectroscopic results (Figure 2), where an increase in intensities was observed on chemical edges when switching the polarization. Across three chemical states, the highest sensitivity to polarization switching was observed on the Ba *M* edge, with a clear average intensity shift to positive values (+0.54). The highest sensitivity observed at the Ba *M* edge correlates to our findings in Figure 2, where a more pronounced modulation on spin–orbit coupling upon polarization switching was observed on Ba *M* compared with other species. Correlation analysis based on joint density plots and Kendall rank correlation (Figure S8) shows that relative changes in any one chemical signal are not systematically related to changes in another signal. This reveals that polarization switching does not lead to the formation of correlated surface features, i.e., Ba–O or Ti–O but rather increases the overall probability of excitations across all surface sites with more sensitivity on Ba sites. This also stands in agreement with our previous findings from the core- and valence-level XPS experiments, where we observed a unique sensitivity on Ba d states upon switching the polarization.[12] It has been previously shown that in the

https://doi.org/10.1021/acsanm.2c05257
ACS Appl. Nano Mater. XXXX, XXX, XXX–XXX

perovskite $BaTiO_3$ structure, Ba sites have a more ionic character compared with Ti sites with valence charges of approximately +2 and +2.5, respectively.[49,50] We believe that the greater ionicity of Ba in the $BaTiO_3$ ferroelectric structure can be a contributing factor for its greater sensitivity to polarization switching as observed in contrast maps. While the positive shifts observed in contrast maps are very well aligned with our earlier observation in single-point XAS measurements, different extents of average shifts observed in the edges (Figure 5j′−l′) could be based on additional factors, such as elemental ionicity,[50] transition matrix element,[51] and local coordination.

In summary, the SX-STM maps reported here exhibit (i) an overall change in the X-ray absorption of surfaces with different polarization directions, in line with the trends observed in single-point XAS measurements, and (ii) local modulation of features a few nanometers in size upon polarization switching (Figure 5). The latter shows that there exists a significant opportunity to resolve the effect of polarization switching on the chemistry of specific atomic sites using SX-STM, if a higher resolution mapping down to sub-nanometer resolution can be achieved, requiring simultaneously excellent probe and surface conditions.

CONCLUSIONS

In this work, we resolved the effect of polarization switching on the X-ray absorption, surface chemistry, and reactivity of ferroelectric $BaTiO_3$ thin films at the nanoscale using SX-STM with possible implications in catalysis. Our experimental results showed that an upward polarization leads to an increase in the number of excitations from core levels to unoccupied states and an overall increase in the absorption spectra across all three Ba *M*, Ti *L*, and O *K* edges, in agreement with our computational XAS calculations based on a multibody BSE formulism. Insight into the catalytic effect of polarization switching was attempted with the adsorption of molecular O_2 both experimentally and computationally, where stronger oxidation on poled-up samples was observed, consistent with stronger orbital hybridization and bonding energies shown by our calculations. Moreover, the effect of surface reconstruction upon polarization switching was studied through chemical mapping of the surfaces, where we observed nanometer-scale features of varying surface chemistry. Pushing *in situ* absorption spectroscopy to the ultimate limit of atomic surface site resolution will help elucidate ferroelectric switching mechanisms and the chemistry of complex interfaces.

ASSOCIATED CONTENT

Supporting Information

The Supporting Information is available free of charge at https://pubs.acs.org/doi/10.1021/acsanm.2c05257.

Additional information, including details of growth and postsynthesis X-ray diffraction, PFM measurements, synchrotron SX-STM measurements, and computational spectroscopy methods (PDF)

AUTHOR INFORMATION

Corresponding Authors

Tod A. Pascal − *Department of NanoEngineering, University of California San Diego, La Jolla, California 92093, United States; Materials Science and Engineering, University of California, San Diego, La Jolla, California 92093, United States;* orcid.org/0000-0003-2096-1143; Email: tpascal@ucsd.edu

David P. Fenning − *Department of NanoEngineering, University of California San Diego, La Jolla, California 92093, United States; Materials Science and Engineering, University of California, San Diego, La Jolla, California 92093, United States;* orcid.org/0000-0002-4609-9312; Email: dfenning@eng.ucsd.edu

Authors

Pedram Abbasi − *Department of NanoEngineering, University of California San Diego, La Jolla, California 92093, United States;* orcid.org/0000-0001-6835-3062

Nozomi Shirato − *Argonne National Laboratory, Lemont, Illinois 60439, United States*

Rishi E. Kumar − *Materials Science and Engineering, University of California, San Diego, La Jolla, California 92093, United States*

Isabel V. Albelo − *Materials Science and Engineering, University of California, San Diego, La Jolla, California 92093, United States;* orcid.org/0000-0002-1798-0223

Matthew R. Barone − *Department of Materials Science and Engineering, Cornell University, Ithaca, New York 14853, United States;* orcid.org/0000-0003-1221-181X

Deniz N. Cakan − *Department of NanoEngineering, University of California San Diego, La Jolla, California 92093, United States*

Ma. de la Paz Cruz-Jáuregui − *Centro de Nanociencias y Nanotecnología (CNyN)-Universidad Nacional Autónoma de México (UNAM) Km 107, Ensenada B.C. C.P. 22800, Mexico;* orcid.org/0000-0002-8407-5741

Sarah Wieghold − *Argonne National Laboratory, Lemont, Illinois 60439, United States*

Darrell G. Schlom − *Department of Materials Science and Engineering, Cornell University, Ithaca, New York 14853, United States; Kavli Institute at Cornell for Nanoscale Science, Ithaca, New York 14853, United States; Leibniz-Institut für Kristallzüchtung, Berlin 12489, Germany;* orcid.org/0000-0003-2493-6113

Volker Rose − *Argonne National Laboratory, Lemont, Illinois 60439, United States*

Complete contact information is available at: https://pubs.acs.org/10.1021/acsanm.2c05257

Author Contributions

P.A., N.S., I.A., and S.W. contributed to experimental data collection. P.A. performed *ab initio* electronic structure and computation XAS calculations. P.A., R.E.K., and D.N.C. performed spectral and chemical mapping processing. M.R.B. performed sample synthesis and XRD characterization with advice from D.G.S. V.R. supervised the experiments at APS beamtime. M.C.J. performed PFM measurements. T.A.P. and D.P.F. supervised computational and experimental efforts, respectively. All of the authors contributed to the manuscript.

Notes

The authors declare no competing financial interest.

ACKNOWLEDGMENTS

This research was primarily supported by the NSF through the UC San Diego Materials Research Science and Engineering Center (UCSD MRSEC), Grant No. DMR-2011924. T.A.P. and D.P.F. acknowledge start-up funding from the Jacob

School of Engineering, UCSD. Materials synthesis was performed in a facility supported by the National Science Foundation [Platform for the Accelerated Realization, Analysis, and Discovery of Interface Materials (PARADIM)] under Cooperative Agreement No. DMR-2039380. M.R.B. and D.G.S. also acknowledge support from the NSF under Cooperative Agreement No. DMR-2039380. Substrate preparation was performed in part at the Cornell NanoScale Facility, a member of the National Nanotechnology Coordinated Infrastructure (NNCI), which is supported by the NSF (Grant No. NNCI-2025233). PFM studies were conducted under Grant CONACYT A1-S-14758 and technical assistance from D. Valdespino and E. Murillo. This work used the Extreme Science and Engineering Discovery Environment (XSEDE) resources Expanse at the San Diego Super Computing Center (SDSC) through allocation CSD622 and DDP381. The use of the Advanced Photon Source, a U.S. Department of Energy Office of Science User Facility, was supported by the U.S. Department of Energy, Office of Science, under Contract No. DE-AC02-06CH11357. This work was performed, in part, at the Center for Nanoscale Materials, a U.S. Department of Energy Office of Science User Facility, and supported by the U.S. Department of Energy, Office of Science, under Contract No. DE-AC02-06CH11357. The authors would also like to thank Dr. David Prendergast from Lawrence Berkley National Lab (LBNL) for helpful discussions on XAS calculations.

REFERENCES

(1) Wu, M. 100 Years of Ferroelectricity. *Nat. Rev. Phys.* **2021**, *3*, 726.
(2) Mikolajick, T.; Slesazeck, S.; Mulaosmanovic, H.; Park, M. H.; Fichtner, S.; Lomenzo, P. D.; Hoffmann, M.; Schroeder, U. Next Generation Ferroelectric Materials for Semiconductor Process Integration and Their Applications. *J. Appl. Phys.* **2021**, *129*, No. 100901.
(3) Scott, J. F. Applications of Modern Ferroelectrics. *Science* **2007**, *315*, 954−959.
(4) Kim, J. Y.; Choi, M.-J.; Jang, H. W. Ferroelectric Field Effect Transistors: Progress and Perspective. *APL Mater.* **2021**, *9*, No. 021102.
(5) Setter, N.; Damjanovic, D.; Eng, L.; Fox, G.; Gevorgian, S.; Hong, S.; Kingon, A.; Kohlstedt, H.; Park, N. Y.; Stephenson, G. B.; Stolitchnov, I.; Taganstev, A. K.; Taylor, D. V.; Yamada, T.; Streiffer, S. Ferroelectric Thin Films: Review of Materials, Properties, and Applications. *J. Appl. Phys.* **2006**, *100*, No. 051606.
(6) Ye, F.; Zhang, Y.; Addiego, C.; Xu, M.; Huyan, H.; Ren, X.; Pan, X. Emergent Properties at Oxide Interfaces Controlled by Ferroelectric Polarization. *npj Comput. Mater.* **2021**, *7*, 130.
(7) Yun, Y.; Mühlenbein, L.; Knoche, D. S.; Lotnyk, A.; Bhatnagar, A. Strongly Enhanced and Tunable Photovoltaic Effect in Ferroelectric-Paraelectric Superlattices. *Sci. Adv.* **2021**, *7*, No. eabe4206.
(8) Butler, K. T.; Frost, J. M.; Walsh, A. Ferroelectric Materials for Solar Energy Conversion: Photoferroics Revisited. *Energy Environ. Sci.* **2015**, *8*, 838−848.
(9) Wan, T. L.; Ge, L.; Pan, Y.; Yuan, Q.; Liu, L.; Sarina, S.; Kou, L. Catalysis Based on Ferroelectrics: Controllable Chemical Reaction with Boosted Efficiency. *Nanoscale* **2021**, *13*, 7096−7107.
(10) Kakekhani, A.; Ismail-Beigi, S. Polarization-Driven Catalysis: Via Ferroelectric Oxide Surfaces. *Phys. Chem. Chem. Phys.* **2016**, *18*, 19676−19695.
(11) Li, Y.; Li, J.; Yang, W.; Wang, X. Implementation of Ferroelectric Materials in Photocatalytic and Photoelectrochemical Water Splitting. *Nanoscale Horiz.* **2020**, *5*, 1174−1187.
(12) Abbasi, P.; Barone, M. R.; de la Paz Cruz-Jáuregui, M.; Valdespino-Padilla, D.; Paik, H.; Kim, T.; Kornblum, L.; Schlom, D. G.; Pascal, T. A.; Fenning, D. P. Ferroelectric Modulation of Surface Electronic States in BaTiO 3 for Enhanced Hydrogen Evolution Activity. *Nano Lett.* **2022**, *22*, 4276−4284.
(13) Abbasi, P.; Fenning, D. P.; Pascal, T. A. Electrocatalytic Hydrogen Evolution on Ferroelectric Perovskite Heterostructures. *ECS Meet. Abstr.* **2022**, 1691.
(14) Walba, D. M.; Stevens, F.; Parks, D. C.; Clark, N. A.; Wand, M. D. Near-Atomic Resolution Imaging of Ferroelectric Liquid Crystal Molecules on Graphite by STM. *Science* **1995**, *267*, 1144−1147.
(15) Pfisterer, J. H. K.; Liang, Y.; Schneider, O.; Bandarenka, A. S. Direct Instrumental Identification of Catalytically Active Surface Sites. *Nature* **2017**, *549*, 74−77.
(16) Wang, J. L.; Pancotti, A.; Jégou, P.; Niu, G.; Gautier, B.; Mi, Y. Y.; Tortech, L.; Yin, S.; Vilquin, B.; Barrett, N. Ferroelectricity in a Quasiamorphous Ultrathin BaTiO3 Film. *Phys. Rev. B* **2011**, *84*, No. 205426.
(17) Datta, S.; Rioult, M.; Stanescu, D.; Magnan, H.; Barbier, A. Manipulating the Ferroelectric Polarization State of BaTiO3 Thin Films. *Thin Solid Films* **2016**, *607*, 7−13.
(18) Barrett, N.; Rault, J.; Krug, I.; Vilquin, B.; Niu, G.; Gautier, B.; Albertini, D.; Lecoeur, P.; Renault, O. Influence of the Ferroelectric Polarization on the Electronic Structure of BaTiO3 Thin Films. *Surf. Interface Anal.* **2010**, *42*, 1690−1694.
(19) Zhu, X. N.; Chen, X.; Tian, H.; Chen, X. M. Atomic Scale Investigation of Enhanced Ferroelectricity in (Ba,Ca)TiO3. *RSC Adv.* **2017**, *7*, 22587−22591.
(20) Kamon-In, O.; Pattanasiriwisawa, W.; Yangthaisong, A.; Srilomsak, S. Structural Studies of Ba1-XLaxTiO3 Using X-Ray Absorption near-Edge Spectroscopy. *J. Phys.: Conf. Ser.* **2009**, *190*, No. 012082.
(21) Jesse, S.; Baddorf, A. P.; Kalinin, S. V. Switching Spectroscopy Piezoresponse Force Microscopy of Ferroelectric Materials. *Appl. Phys. Lett.* **2006**, *88*, No. 062908.
(22) Pan, X.; Li, L.-Z.; Xu, M.; Dai, S.; Blum, T. In Situ TEM Probing of Ferroelectric Switching under Electrical Bias. *Microsc. Microanal.* **2018**, *24*, No. 1812.
(23) Gao, P.; Nelson, C.; Jokisaari, J.; Baek, S.; Eom, C.; Wang, E.; Pan, X. In Situ TEM Studies of Ferroelectric Thin Films. *Microsc. Microanal.* **2011**, *17*, No. 1362.
(24) Zheng, Y.; Zhong, C.; Zheng, Y.; Gao, Z.; Cheng, Y.; Zhong, Q.; Liu, C.; Wang, Y.; Qi, R.; Huang, R.; Lyu, H. In *In Situ Atomic Visualization of Structural Transformation in Hf0.5Zr0.5O2 Ferroelectric Thin Film: From Nonpolar Tetragonal Phase to Polar Orthorhombic Phase*, Digest of Technical Papers—Symposium on VLSI Technology, 2021.
(25) Conroy, M.; Moore, K.; O'Connell, E.; Courtney, E.; Harvey, A.; Cochard, C.; Guy, J.; McQuaid, R.; Jones, L.; Downing, C.; Whatmore, R.; Gregg, M.; Bangert, U. Investigating Ferroelectric Domain and Domain Wall Dynamics at Atomic Resolution by TEM/STEM in Situ Heating and Biasing. *Microsc. Microanal.* **2019**, *25*, No. 1882.
(26) Li, L.; Xie, L.; Pan, X. Real-Time Studies of Ferroelectric Domain Switching: A Review. *Rep. Prog. Phys.* **2019**, *82*, No. 126502.
(27) Mun, J.; Peng, W.; Roh, C. J.; Lee, S.; Matsumura, S.; Lee, J. S.; Noh, T. W.; Kim, M. In Situ Cryogenic HAADF-STEM Observation of Spontaneous Transition of Ferroelectric Polarization Domain Structures at Low Temperatures. *Nano Lett.* **2021**, *21*, No. 8679.
(28) Hong, L.; Huber, D.; Contreras-Guerrero, R.; Droopad, R.; Klie, R. F. In-Situ STEM-EELS Observation of Ferroelectric Switching of BaTiO 3 Film on GaAs. *Microsc. Microanal.* **2017**, *23*, 1628−1629.
(29) Rose, V.; Shirato, N.; Bartlein, M.; Deriy, A.; Ajayi, T.; Rosenmann, D.; Hl, S. W.; Fisher, M.; Reininger, R. XTIP—The World's First Beamline Dedicated to the Synchrotron X-Ray Scanning Tunneling Microscopy Technique. *J. Synchrotron Radiat.* **2020**, *27*, 836−843.
(30) Rose, V.; Wang, K.; Chien, T.; Hiller, J.; Rosenmann, D.; Freeland, J. W.; Preissner, C.; Hla, S. W. Synchrotron X-Ray Scanning Tunneling Microscopy: Fingerprinting near to Far Field Transitions

https://doi.org/10.1021/acsanm.2c05257
ACS Appl. Nano Mater. XXXX, XXX, XXX−XXX

on Cu(111) Induced by Synchrotron Radiation. *Adv. Funct. Mater.* **2013**, *23*, 2646−2652.
(31) Shirato, N.; Cummings, M.; Kersell, H.; Li, Y.; Stripe, B.; Rosenmann, D.; Hla, S.-W.; Rose, V. Elemental Fingerprinting of Materials with Sensitivity at the Atomic Limit. *Nano Lett.* **2014**, *14*, 6499−6504.
(32) Gilmore, K.; Pelliciari, J.; Huang, Y.; Kas, J. J.; Dantz, M.; Strocov, V. N.; Kasahara, S.; Matsuda, Y.; Das, T.; Shibauchi, T.; Schmitt, T. Description of Resonant Inelastic X-Ray Scattering in Correlated Metals. *Phys. Rev. X* **2021**, *11*, No. 031013.
(33) Blase, X.; Duchemin, I.; Jacquemin, D.; Loos, P. F. The Bethe-Salpeter Equation Formalism: From Physics to Chemistry. *J. Phys. Chem. Lett.* **2020**, *11*, 7371−7382.
(34) Vinson, J.; Rehr, J. J.; Kas, J. J.; Shirley, E. L. Bethe-Salpeter Equation Calculations of Core Excitation Spectra. *Phys. Rev. B* **2011**, *83*, No. 115106.
(35) Dvorak, M.; Baumeier, B.; Golze, D.; Leppert, L.; Rinke, P. Editorial: Many-Body Green's Functions and the Bethe-Salpeter Equation in Chemistry: From Single Molecules to Complex Systems. *Front. Chem.* **2022**, *10*, No. 866492.
(36) Lee, M. C.; Lee, S.; Won, C. J.; Lee, K. D.; Hur, N.; Chen, J. L.; Cho, D. Y.; Noh, T. W. Hybridized Orbital States in Spin-Orbit Coupled 3d-5d Double Perovskites Studied by x-Ray Absorption Spectroscopy. *Phys. Rev. B* **2018**, *97*, No. 125123.
(37) Tenne, D. A.; Bruchhausen, A.; Lanzillotti-Kimura, N. D.; Fainstein, A.; Katiyar, R. S.; Cantarero, A.; Soukiassian, A.; Vaithyanathan, V.; Haeni, J. H.; Tian, W.; Schlom, D. G.; Choi, K. J.; Kim, D. M.; Eom, C. B.; Sun, H. P.; Pan, X. Q.; Li, Y. L.; Chen, L. Q.; Jia, Q. X.; Nakhmanson, S. M.; Rabe, K. M.; Xi, X. X. Probing Nanoscale Ferroelectricity by Ultraviolet Raman Spectroscopy. *Science* **2006**, *313*, No. 1614.
(38) Wen, Z.; Li, C.; Wu, D.; Li, A.; Ming, N. Ferroelectric-Field-Effect-Enhanced Electroresistance in Metal/Ferroelectric/Semiconductor Tunnel Junctions. *Nat. Mater.* **2013**, *12*, 617−621.
(39) Theis, C. D.; Schlom, D. G. Cheap and Stable Titanium Source for Use in Oxide Molecular Beam Epitaxy Systems. *J. Vac. Sci. Technol., A* **1996**, *14*, 2677−2679.
(40) de Groot, F.; Kotani, A.*Core Level Spectroscopy of Solids*; CRC Press, 2008.
(41) Fuentes-Cobas, L. E.; Montero-Cabrera, M. E.; Pardo, L.; Fuentes-Montero, L. Ferroelectrics under the Synchrotron Light: A Review. *Materials* **2016**, *9*, No. 14.
(42) Nakamura, T.; Oike, R.; Kimura, Y.; Tamenori, Y.; Kawada, T.; Amezawa, K. Operando Soft X-Ray Absorption Spectroscopic Study on a Solid Oxide Fuel Cell Cathode during Electrochemical Oxygen Reduction. *ChemSusChem* **2017**, *10*, 2008−2014.
(43) Torgersen, J.; Acharya, S.; Dadlani, A. L.; Petousis, I.; Kim, Y.; Trejo, O.; Nordlund, D.; Prinz, F. B. Relating Electronic and Geometric Structure of Atomic Layer Deposited BaTiO3 to Its Electrical Properties. *J. Phys. Chem. Lett.* **2016**, *7*, 1428−1433.
(44) Bugnet, M.; Radtke, G.; Woo, S. Y.; Zhu, G. Z.; Botton, G. A. Temperature-Dependent High Energy-Resolution EELS of Ferroelectric and Paraelectric BaTiO3 Phases. *Phys. Rev. B* **2016**, *93*, 1−5.
(45) Clancy, J. P.; Chen, N.; Kim, C. Y.; Chen, W. F.; Plumb, K. W.; Jeon, B. C.; Noh, T. W.; Kim, Y. J. Spin-Orbit Coupling in Iridium-Based 5d Compounds Probed by x-Ray Absorption Spectroscopy. *Phys. Rev. B* **2012**, *86*, 1−8.
(46) Mastelaro, V. R.; Neves, P. P.; Michalowicz, A.; Eiras, J. A. Electronic Structure of Pb1-XBaxZr 0.65Ti0.35O3 Ferroelectric Compounds Probed by Soft x-Ray Absorption Spectroscopy. *J. Phys.: Condens. Matter* **2007**, *19*, 8−16.
(47) Fleming, L.; Fulton, C. C.; Lucovsky, G.; Rowe, J. E.; Ulrich, M. D.; Lüning, J. Local Bonding Analysis of the Valence and Conduction Band Features of TiO2. *J. Appl. Phys.* **2007**, *102*, No. 033707.
(48) Kas, J. J.; Vinson, J.; Trcera, N.; Cabaret, D.; Shirley, E. L.; Rehr, J. J. Many-Pole Model of Inelastic Losses Applied to Calculations of XANES. *J. Phys.: Conf. Ser.* **2009**, *190*, No. 012009.
(49) Sousa, C.; Franccsc, I. Ionic-Covalent Transition in Titanium Oxides Carmcn. *Phys. Rev. B* **1989**, *50*, 974−981.
(50) Bocquet, A. E.; Mizokawa, T.; Morikawa, K.; Fujimori, A.; Barman, S. R.; Maiti, K.; Sarma, D. D.; Tokura, Y.; Onoda, M. Electronic Structure of Early 3 d -Transition-Metal Oxides by Analysis of the 2 p Core-Level Photoemission Spectra. *Phys. Rev. B* **1996**, *53*, 1161−1170.
(51) Henderson, G. S.; Groot, F. M. F.; De Moulton, B. J. A. X-Ray Absorption Near-Edge Structure (XANES) Spectroscopy. *Rev. Mineral. Geochem.* **2014**, *78*, 75−138.

https://doi.org/10.1021/acsanm.2c05257
ACS Appl. Nano Mater. XXXX, XXX, XXX−XXX